LANGMUIR

pubs.acs.org/Langmuir Article

Characterization of Ligand Adsorption at Individual Gold Nanocubes

Myung-Hoon Choi, Soojin Jeong, Yi Wang, Sang-Joon Cho, Sang-Il Park, Xingchen Ye,* and Lane A. Baker*

Cite This: *Langmuir* 2021, 37, 7701−7711 Read Online

ACCESS | Metrics & More | Article Recommendations | Supporting Information

ABSTRACT: Cetyltrimethylammonium bromide (CTAB) is a widely used surfactant that aids the aqueous synthesis of colloidal nanoparticles. However, the presence of residual CTAB on nanoparticle surfaces can significantly impact nanoparticle applications, such as catalysis and sensing, under hydrated conditions. As such, consideration of the presence and quantity of CTAB on nanoparticle surfaces under hydrated conditions is of significance. Herein, as part of an integrated material characterization framework, we demonstrate the feasibility of in situ atomic force microscopy (AFM) to detect CTAB on the surface of Au nanocubes (Au NCs) under hydrated conditions, which enabled superior characterization compared to conventional spectroscopic methods. In situ force−distance (FD) spectroscopy and Kelvin probe force microscopy (KPFM) measurements support additional characterization of adsorbed CTAB, while correlative in situ AFM and scanning electron microscopy (SEM) measurements were used to evaluate sequential steps of CTAB removal from Au NCs across hydrated and dehydrated environments, respectively. Notably, a substantial quantity of CTAB remained on the Au NC surface after methanol washing, which was detected in AFM measurements but was not detected in infrared spectroscopy measurements. Subsequent electrochemical cleaning was found to be critically important to remove CTAB from the Au NC surface. Correlative measurements were also performed on individual nanoparticles, which further validate the method described here as a powerful tool to determine the extent and degree of CTAB removal from nanoparticle surfaces. This AFM-based method is broadly applicable to characterize the presence and removal of ligands from nanomaterial surfaces under hydrated conditions.

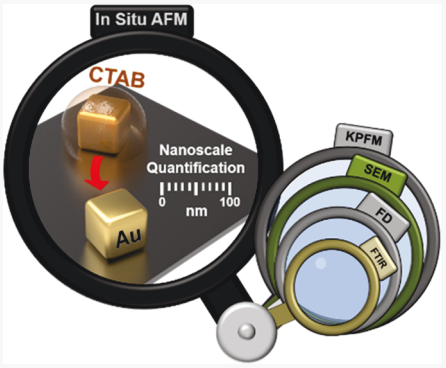

INTRODUCTION

Solution-based synthesis can achieve exquisite control of complex physical and chemical properties of nanoscale materials.[1] Surface-adsorbed ligands or surfactants, such as cetyltrimethylammonium bromide (CTAB),[2−4] are frequently used in metal nanocrystal synthesis to favor the growth of certain crystal orientations.[5,6] One such example is the synthesis of faceted Au nanocrystals by seed-mediated growth in the presence of CTAB, which has been used as a model system for understanding nanocrystal growth kinetics and shape control. While ligands are useful in controlled nanocrystal synthesis, the presence of ligands is an important consideration in subsequent applications, especially where surface reactivity or structure−function relationships are of interest. For instance, Thoi and Hall reported bias-induced reorganization of interfacial CTAB during electrocatalysis at Cu surfaces promoted CO_2 reduction and suppressed H_2 evolution.[7,8] Ligand-promoted selectivity in electrocatalysis has also been reported in nanoparticle systems.[9,10] In other examples, especially in particle-based systems where ligands are integral in sample preparation, the effects of ligands (including CTAB) on subsequent applications have been less well studied.[6] We recently found that residual CTAB on Au nanocubes (NCs) complicated quantitation in nanoscale electrochemical imaging experiments and required special attention.[11] Thus, routes to characterize the presence of residual ligands and to understand interfacial chemistry at the single-nanocrystal level are highly desirable.[12]

CTAB adsorption at surfaces has been previously studied in detail, by means of in situ atomic force microscopy (AFM),[13] force−distance (FD) spectroscopy,[14,15] and electron microscopy (EM).[16,17] Specifically, Lamont and Ducker used in situ AFM imaging and FD spectroscopy to probe morphology and thickness of CTAB adsorbed on mica.[14] Huang and co-workers studied adsorbed CTAB via aberration-corrected scanning transmission electron microscopy with electron energy loss spectroscopy (STEM-EELS)[16] and revealed the presence of a thin layer of CTAB at the nanoparticle surface. In another report, Kotov and co-workers visualized asymmetrically

Received: March 12, 2021
Revised: May 4, 2021
Published: June 18, 2021

https://doi.org/10.1021/acs.langmuir.1c00694
Langmuir 2021, 37, 7701−7711

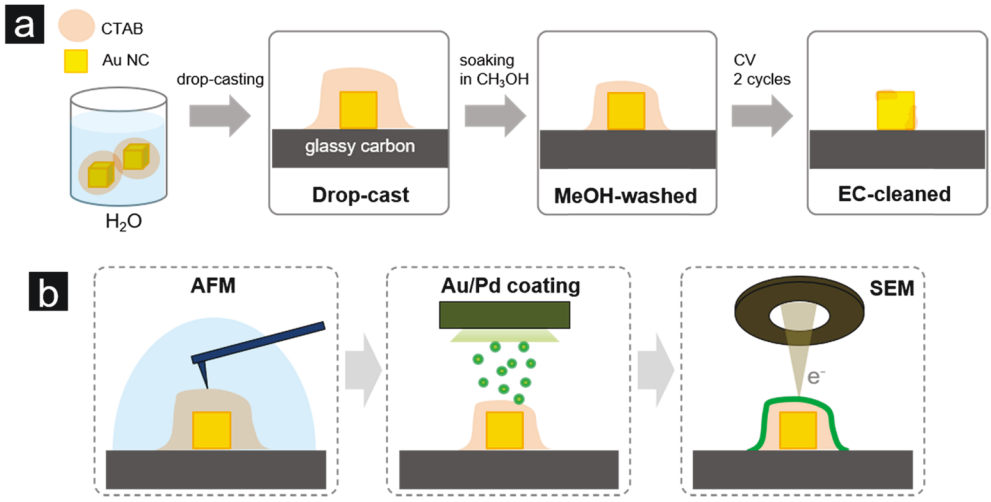

Figure 1. (a) Idealized schematic of the sequential CTAB removal process on Au NC samples. An aqueous CTAB-capped Au NC solution (in the presence of excess CTAB) was drop-cast on a GC substrate, followed by sequential washing with methanol (MeOH-washed) and electrochemical cleaning (EC-cleaning). (b) Workflow of nanoscale measurements to characterize CTAB adsorption on single Au NCs. A Au NC sample was measured via in situ AFM under H_2O. A Au/Pd layer was then sputter-coated on the Au NC sample, followed by SEM measurement under dehydrated conditions.

adsorbed CTAB on Au nanocrystals by carbon elemental mapping via energy-filtered transmission electron microscopy (TEM).[17]

Notably, for previous studies, electron microscopy and in situ AFM represent a vacuum vs solution dichotomy in the interfacial environment. Here, we bridge this gap, by characterizing CTAB at the interface of nanocrystals in both hydrated and vacuum environments, ultimately comparing the same individual nanocrystal. Samples are prepared by drop-casting, and the effects of methanol washing and of subsequent electrochemical cycling[18−20] to remove adsorbed CTAB are investigated. Specifically, highly monodisperse Au NCs that enable quantitative comparison of particle dimensions have been examined with correlative in situ AFM and scanning electron microscopy (SEM) measurements. The initial presence of CTAB on Au NCs is characterized, and compelling evidence for the removal of CTAB after cleaning is observed. Results here add to the growing repertoire of nanoscale characterization of synthesized nanomaterials and underscores the importance of multiple tools from measurements in electrochemistry[21,22] and other fields[23−27] to assess nanomaterial quality and cleanliness. We show that correlative approaches prove especially informative at bridging the gap between high-resolution ex situ measurements and in situ studies that more closely mimic in operando conditions for electrochemical measurements.

EXPERIMENTAL SECTION

Chemicals. Hydrogen tetrachloroaurate trihydrate ($HAuCl_4 \cdot 3H_2O$, ≥99.9% trace metals basis), sodium borohydride ($NaBH_4$, 99%), silver nitrate ($AgNO_3$, ≥99.0%), L-ascorbic acid (≥99.5%), hydrochloric acid (HCl, 37%), and nitric acid (HNO_3, 70%) were purchased from Sigma-Aldrich. Hexadecyltrimethylammonium bromide (CTAB, >98.0%) and hexadecylpyridinium chloride monohydrate (CPC, >98.0%) were purchased from TCI America. Potassium bromide (KBr, 99.999%) was purchased from Acros Organics. All chemicals were used as received without further purification. Ultrapure water (18.2 MΩ·cm at 25 °C) obtained from a Milli-Q (MilliporeSigma) water purification system was used in all experiments. All glassware for nanocrystal synthesis was cleaned with aqua regia (a mixture of HCl and HNO_3 in 3:1 volume ratio) and rinsed thoroughly with water before use.

Synthesis of Au Nanocubes. Au nanocubes (NCs) were synthesized by a previously reported seed-growth method with slight modifications.[28] First, 19 nm seed Au nanospheres were synthesized by iterative oxidative dissolution and reductive growth of Au nanorods (NRs) developed by the Mirkin group (see details in the Supporting Information) with slight modifications.[29] Then, 19 nm seed particles were redispersed in 100 mM CPC solution to attain an optical density (OD) of 1.0. Then, 750 μL of the seed solution was introduced to the growth solution which consisted of a mixture of 25 mL of 100 mM CPC, 2.5 mL of 100 mM KBr, 1.5 mL of 10 mM $HAuCl_4$, and 2.25 mL of 100 mM L-ascorbic acid solutions. The final solution was kept undisturbed for 1 h. As-synthesized Au NCs were precipitated by centrifugation at 3000 rpm for 3 min and redispersed in 25 mL of 50 mM CTAB solution and centrifuged again at 3000 rpm for 3 min. Au NCs were finally dispersed pure water to attain an OD of 45. Au NCs utilized in this work had an edge length of 77.5 ± 2.0 nm with an aspect ratio of 1.03 ± 0.03, determined from automated TEM image analysis with Matlab (Figures S1 and S2).

Deposition of Au NCs onto Glassy Carbon Substrates. Typically, a glassy carbon (GC) substrate (1.2 cm × 2.4 cm, 99.99%, Alfa Aesar) was soaked in aqua regia for 1 min to remove any metal impurities. After rinsing with copious amounts of water, the substrate was mechanically polished with alumina powder (CH Instruments) in order of decreasing particle size (1.0 μm followed by 0.5 and 0.05 μm). The polished substrate was then further cleaned by sonication (1 min duration) with a 1:1 (v/v) mixture of water and isopropanol, followed by a second sonication (1 min duration) in acetone. After blow-drying with N_2, the GC substrate was further polished against a clean, wet polishing pad to remove residual alumina particles. Finally, 20 μL of the Au NC solution (OD: 0.6, obtained by diluting the stock solution 75 times with DI H_2O) was drop-cast onto the prepared GC substrate. Samples were allowed to dry fully prior to subsequent steps.

Methanol Cleaning. Au NC-deposited GC substrates were immersed in methanol for 2 min to remove CTAB, driven by the higher solubility of CTAB in methanol than in water.[30−32] Efficacy of CTAB removal was monitored by Fourier transform infrared spectroscopy (FTIR) through the intensity of symmetric (~2849 cm^{-1}) and asymmetric (~2914 cm^{-1}) C−H stretching vibrations (Figure S3). Typically, C−H signals became negligible after 2 min of methanol treatment.

Electrochemical Cleaning. Cyclic voltammetry (CV) was utilized to remove residual CTAB from methanol-washed Au NCs

https://doi.org/10.1021/acs.langmuir.1c00694
Langmuir 2021, 37, 7701−7711

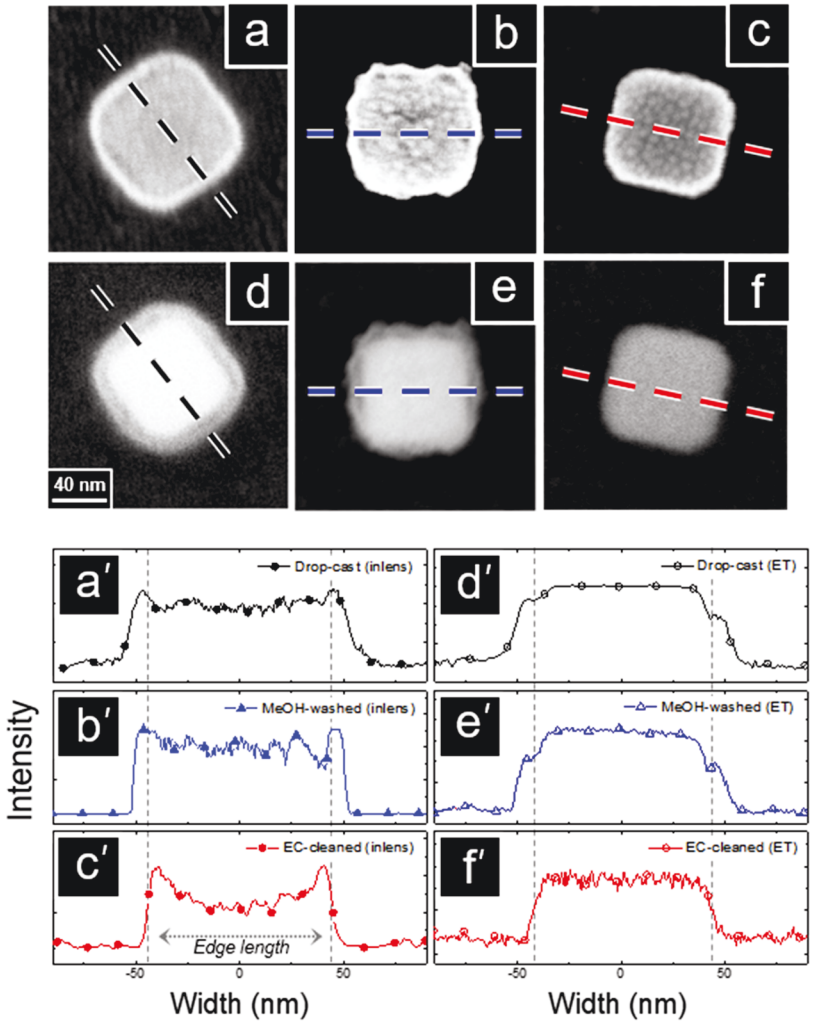

Figure 2. Representative electron micrographs of drop-cast (a, d), MeOH-washed (b, e), and EC-cleaned (c, f) Au NCs after Au/Pd sputter coating. SEM images (a–c) were obtained with an in-lens detector, while (d–f) were obtained with an Everhart–Thornley (ET) detector. Corresponding line profiles from the midsection of each image (a′–f′). The dashed line indicates nanoparticle edge length measured from transmission electron microscopy. The scale bar in (d) is applied to all SEM images.

and the GC substrate. A custom-built three-electrode setup was used,[11] with the GC substrate, platinum gauze (52 mesh woven from 0.1 mm diameter Pt wire, 99.9%, Alfa Aesar), and Ag/AgCl (3.5 M NaCl, BASi) serving as the working, counter, and reference electrodes, respectively. The working electrode area was defined by a Teflon cell with an opening isolated by an O-ring. Electrochemical measurements were carried out on a potentiostat (SP-300, Biologic) with 100 mM $HClO_4$ (Acros Organics) supporting electrolyte. The working electrode potential was swept from 0 to −1.0 V vs Ag/AgCl (3.5 M NaCl) at a scan rate of 100 mV/s for two cycles.

Workflow for Au-Nanocube-on-GC Samples. Figure 1a illustrates the general workflow to remove CTAB, consisting of three steps: drop-casting, methanol washing, and electrochemical cleaning (voltammetric cycling). At least three independent samples with nearly identical surface coverage were prepared by drop-casting colloidal Au NC solutions onto GC substrates. To investigate CTAB removal at each cleaning step described above, three freshly prepared Au NC samples were used. The first sample, referred to as "drop-cast Au NC," was examined without any additional treatment. The remaining two samples were then immersed in methanol for 2 min. The second sample, referred to as "MeOH-washed Au NC," was stopped at this step. The last sample, referred to as "EC-cleaned Au NC," was further treated via two cycles of cyclic voltammetry from 0 to −1.0 V vs Ag/AgCl in 0.1 M $HClO_4$. The presence of adsorbates was assessed for each Au NC sample via sequential measurements of in situ atomic force microscopy (AFM) and scanning electron microscopy (SEM), as illustrated in Figure 1b. Prepared samples were initially measured with in situ AFM to probe the presence of CTAB under hydrated conditions. After AFM measurements including FD, samples were dried for Kelvin probe force microscopy (KPFM) measurement. Samples were then sputter-coated with a thin Au/Pd layer, followed by SEM measurement to characterize samples under dehydrated conditions.

Electron Microscopy. Transmission electron microscope (TEM) images were recorded on a JEOL JEM 1010 microscope operating at 80 kV with a tungsten filament. TEM samples were prepared by drop-casting ca. 10 μL of Au NC solution onto a 300-mesh carbon-coated copper grid (Ted Pella). Scanning electron microscope (SEM) images were obtained on an Auriga FIB-SEM microscope equipped with in-lens and Everhart–Thornley (ET) detectors at 20 kV of electron high tension (EHT), 30 μm of aperture size, and 5.7–6.0 mm of working distance. Samples were sputter-coated with a conductive Au/Pd layer to mitigate charging during SEM imaging. Line profile analysis of electron micrographs was performed with ImageJ (NIH).[33]

In Situ AFM. The topography of Au NCs in H_2O was obtained by AFM (XE-Bio, Park Systems). Prior to topography acquisition, piezoelectric scanners were calibrated with a standard sample, TGQ1 (NT-MDT). Au NC samples were imaged in H_2O, in a liquid cell sealed by a silicon cover to prevent evaporation and reduce thermal drift (Figure S4). Soft tapping mode was conducted in situ with an

https://doi.org/10.1021/acs.langmuir.1c00694
Langmuir 2021, 37, 7701−7711

amplitude of 5−10 nm at 25−30 kHz resonance frequency. The softness (spring constant: 0.1 N/m) of the cantilever (BL-AC40TS, Olympus) and small dimension of the cantilever (length 38 μm and width 16 μm) and tip (ca. 10 nm radius) used here provide sufficient sensitivity for imaging in hydrated conditions with high topographical resolution.[24,34−36] Topography data was analyzed by XEI software (Park Systems)[37,38] and Gwyddion.[39] Tip-deconvolution analysis of AFM topography was conducted via ProfilmOnline (KLA)[40] (for details of tip-deconvolution, see the Results and Discussion section).

Force−Distance (FD) Spectroscopy. The topographic images of Au NCs from in situ AFM imaging provided X and Y coordinates at features of interest with nanometer-scale precision. FD spectroscopy and FD mapping were performed at positions where individual Au NCs were located. The following parameters were used to obtain FD curves: 1.0−1.5 nN force limit, 1.0 μm/s approach and retract velocity, and 1.0 μm vertical tip displacement. In advance of FD curve acquisition, the laser reflection sensitivity was calibrated from an FD curve obtained in situ at a clean GC substrate. Positional errors originating from thermal drift were carefully corrected by the repetitive acquisition of AFM topography at the same sample area.

Kelvin Probe Force Microscopy (KPFM). KPFM was performed with an AFM (NX-10, Park Systems) to measure contact potential difference (CPD) between the tip and sample. Samples for KPFM measurement were prepared in the same way as those used for in situ AFM measurement. Conductive cantilevers, NCS36 Cr-Au (Mikromasch), with tip diameter ca. 30 nm, typical spring constant 2 N/m, resonance frequency 130 kHz, and total tip height 12−18 μm were used. KPFM images and corresponding topographies of samples were obtained simultaneously. CPD was measured by modulation of an AC bias 0.5 V in amplitude at 3 kHz. All KPFM measurements were carried out under ambient conditions.

RESULTS AND DISCUSSION

SEM Measurements. Electron microscopy is a routine and widely accepted method for the analysis of nanoparticles. In measurements here, a thin Au/Pd layer was sputter-coated on each of three Au NC samples. In the absence of a sputter-coated metal layer, adsorbed CTAB underwent significant charging and morphological transformation (Figure S5) when exposed to the electron beam. CTAB thickness was determined by subtracting the Au/Pd thin layer thickness (Figures S6 and S7) from the overall thickness of the outer layer, which presumably consists of both Au/Pd and CTAB. Typically, CTAB and the core Au NC could be distinguished by SEM due to contrast differences, thereby allowing measurement of a composite layer that represented the combined thickness of Au/Pd coating and CTAB from electron micrographs (Figure S8). The composite layer shows two regions of differing contrast. The brighter outermost layer is taken to consist of the Au/Pd coating and CTAB, and the darker region to be comprised primarily of CTAB, which produces lower contrast due to lower conductivity. The apparent thickness of the Au/Pd layer (for all coatings) is consistently ∼5 nm; however, the possibility of intermixing between the CTAB layer and Au/Pd coating cannot be explicitly ruled out. For the EC-cleaned sample, where most CTAB appeared to be removed, the difference in thickness measured before and after Au/Pd coating was taken as the thickness of the Au/Pd layer.

SEM images were used to visualize the thickness of CTAB on the sidewall of Au NCs (Figure 2a−f) in dehydrated conditions. To resolve the core Au NC from adsorbed CTAB, each Au NC was measured separately via the in-lens detector (Figure 2a−c) and Everhart−Thornley (ET) detector (Figure 2d−f). Drop-cast and EC-cleaned Au NCs showed well-resolved surfaces with the in-lens detector (Figure 2a,c), while the contrast difference of CTAB for the MeOH-washed Au NCs was more apparent with the ET detector (Figure 2e). The line profile of intensity collected from drop-cast (black line), MeOH-washed (blue line), and EC-cleaned Au NCs (red line) indicated the approximate in vacuo width of adsorbed CTAB on Au NCs (Figure 2a′−f′). Measured widths of drop-cast, MeOH-washed, and EC-cleaned samples were ca. 100, 97, and 89 nm, respectively (Figures S9−S12 and Tables S1−S3), indicating that subsequent cleaning steps decreased the amount of CTAB on Au NCs. Consequently, CTAB thicknesses of drop-cast and MeOH-washed Au NC were 4.2 ± 1.6 and 3.0 ± 1.3 nm, respectively. CTAB was not clearly observed for EC-cleaned Au NCs, suggesting most of CTAB was removed. Summarized measured values are presented in Table 1.

Table 1. Calculated Thickness of CTAB at Au NCs from SEM Measurement[a]

	n	CTAB average thickness (nm)	Au/Pd coating thickness (nm)
drop-cast	5	4.2 ± 1.6	5.1
MeOH-washed	8	3.0 ± 1.3	5.6
EC-cleaned	7	not detectable	5.1

[a]CTAB thickness was determined by subtracting the estimated thickness of the Au/Pd layer from measured widths (n: number of Au NCs analyzed). Details are included in Tables S1−S3.

AFM Measurements. The morphology of CTAB adsorbed on Au NCs under hydrated conditions was examined with in situ AFM. Figure 3a−f shows two-dimensional (2D) and three-dimensional (3D)-rendered topographic images of Au NCs, respectively. Line profiles at locations indicated by dashed lines on drop-cast (black line), MeOH-washed (blue line), and EC-cleaned Au NCs (red line) are shown in Figure 3g. The three different Au NC samples show a clear trend of decreasing thickness of CTAB on Au NCs. The apparent height and full width at half-maximum (FWHM) values can be determined from line profiles (Figures S13−S15 and Tables S4−S6). Drop-cast Au NCs showed a height of 87.4 ± 3.2 nm with FWHM of 233.5 ± 58.4 nm, MeOH-washed Au NCs showed 79.6 ± 3.1 nm height with FWHM of 135.6 ± 6.5 nm, and EC-cleaned Au NCs showed 78.8 ± 3.7 nm height with FWHM of 103.5 ± 5.1 nm (Figure 3h,i). Importantly, for this data, maximum height measurements are expected to be accurate reflections of the true sample height, while FWHM measurements represent a convolution of imaging artifacts (vide infra).

Compared to the 77.5 ± 2.0 nm edge length of Au NCs measured by TEM analysis, the drop-cast sample showed ca. 10 and 156 nm greater maximum height and FWHM, respectively (Table 2), suggesting that a substantial amount of CTAB was initially present on Au NCs. Notably, the height of Au NCs decreased by ca. 9 and 10%, and the FWHM decreased by ca. 42 and 56% after subsequent MeOH-washing and EC-cleaning steps, respectively. Removal of CTAB by methanol treatment is presumed to occur due to a difference in solubility of CTAB between methanol and water.[30−32] The lower dielectric constant of MeOH (relative to water) might also screen charges less effectively, leading to destabilization of CTAB−CTAB interactions. Considering a nominal 77.5 nm edge length of the original Au NC, and a standard deviation of ±2.0 nm in that measurement, a difference of 1.3 nm in height

https://doi.org/10.1021/acs.langmuir.1c00694
Langmuir 2021, 37, 7701−7711

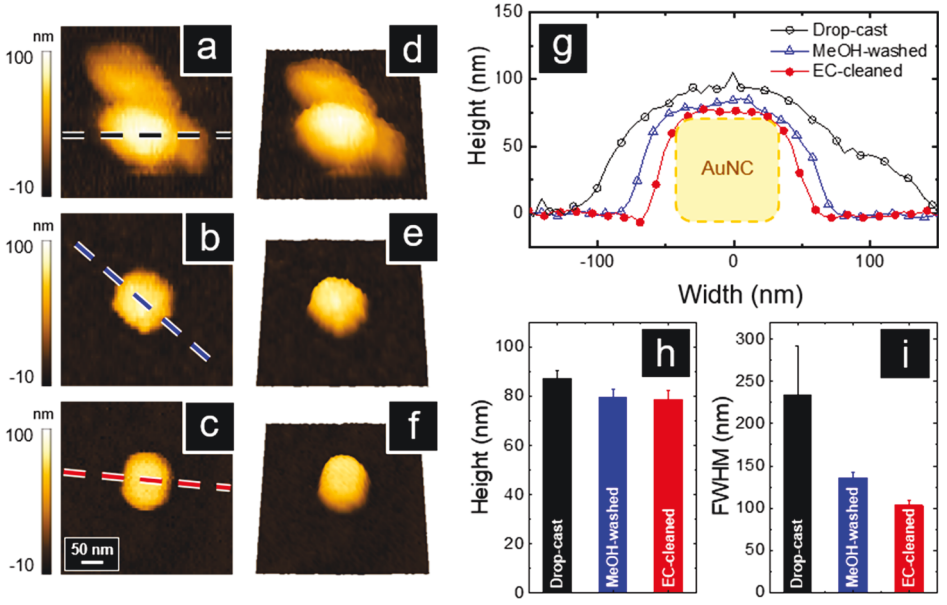

Figure 3. Representative in situ AFM topographies (a–c) and corresponding 3D-rendered topographies (d–f) of drop-cast (a, d), MeOH-washed (b, e), and EC-cleaned (c, f) Au NCs. Line profiles of the three samples measured from each corresponding in situ AFM topography (g): drop-cast (black trace), MeOH-washed (blue trace), and EC-cleaned Au NCs (red trace). An outline of a Au NC size is included, based on an edge length (ca. 77.5 nm, yellow-dashed line). Average maximum height (h) and average FWHM (i) measured from each sample shown in (a–f). The scale bar in (c) is applied to all AFM topographies.

Table 2. Average Maximum Height and FWHM of Au NCs from Three Samples Measured by In Situ AFM in H_2O (*n*: Number of Au NCs Measured)

	n	maximum height (nm)	FWHM (nm)
drop-cast	8	87.4 ± 3.2	233.5 ± 58.4
MeOH-washed	8	79.6 ± 3.1	135.6 ± 6.5
EC-cleaned	6	78.8 ± 3.7	103.5 ± 5.1

Table 3. Summary of Approximate Yield Force, Maximum Adhesion Force, and Interaction Start Distance between Drop-Cast and MeOH-Washed Au NCs Obtained from FD Curves in Figure 4

	yield force (nN)	max. adhesion force (nN)	interaction start distance (nm)
drop-cast	ca. 0.7	ca. −0.5	ca. 80
MeOH-washed	ca. 0.2	ca. −0.2	ca. 40
EC-cleaned	N/A	N/A	N/A

and 26 nm in FWHM after the EC-cleaning step suggests that the treatment protocol employed here removes the majority of CTAB on Au NCs. For EC-cleaning, the use of acidic media and excursions to potentials suitable for proton reduction generates surface adsorption/desorption of protons/H_2, which likely aids in disrupting the adsorption of CTAB. This supposition is in line with previous reports that have described CTAB reorganization at metal surfaces under an applied potential.[8] Additionally, Fan and co-workers reported a similar electrochemical cleaning procedure that utilized proton reduction in 0.1 M $HClO_4$ for disrupting adsorption of oleylamine at Pt nanoparticles.[20]

Differences in Au NC dimensions measured by AFM, especially for the MeOH-washed and EC-cleaned sample heights, are difficult to confirm, and as such additional characterization approaches were employed. Force–distance (FD) spectroscopy can detect adsorbed CTAB with higher sensitivity than AFM imaging because the cantilever tip vertically probes a point on the surface of the particle without feedback. The yield force (Table 3) measured at a typical drop-cast Au NC was ca. 0.7 nN (ⓑ in Figure 4a), and for a MeOH-washed Au NC was ca. 0.2 nN (ⓔ in Figure 4b). The maximum adhesion force obtained from drop-cast Au NCs was ca. −0.5 nN (ⓒ in Figure 4a), which is about 2.5 times larger than that measured from MeOH-washed Au NCs (ⓕ in Figure 4b). When considered in the context of AFM imaging and SEM experiments, these results suggest that the majority of the layer of CTAB at the interface of drop-cast Au NCs is removed with MeOH washing, but residual CTAB remains.

Yield and adhesion forces were not detected in EC-cleaned Au NCs, suggesting that CTAB was removed from the surface of EC-cleaned Au NCs. These results are in line with those observed from SEM measurements in which CTAB appeared rougher and thinner after methanol treatment and was not observed after electrochemical cycling. Tip–interface interactions were measured at distances of ca. 80 nm for drop-cast Au NCs (ⓐ in Figure 4a), and ca. 40 nm for MeOH-washed Au NCs (ⓓ in Figure 4b), while EC-cleaned Au NCs showed no interaction. The starting points for interactions in FD curves were confirmed by comparing the difference between approach and retract curves.

Potentials measured by KPFM were used to demonstrate both the effects of residual CTAB and the effect of cleaning as described here on the electrical properties of Au NCs. In the KPFM image of drop-cast Au NCs (Figure 5a), CPD was not apparent while CPD values were of ca. −50 mV (Figure 5b) and −90 mV (Figure 5c) in MeOH-washed and EC-cleaned Au NCs, respectively. Topographic images collected simultaneously showed features consistent with nanoparticle dimensions, although Au NCs are difficult to definitively identify in drop-cast samples (Figure 5d–f).

https://doi.org/10.1021/acs.langmuir.1c00694
Langmuir 2021, 37, 7701−7711

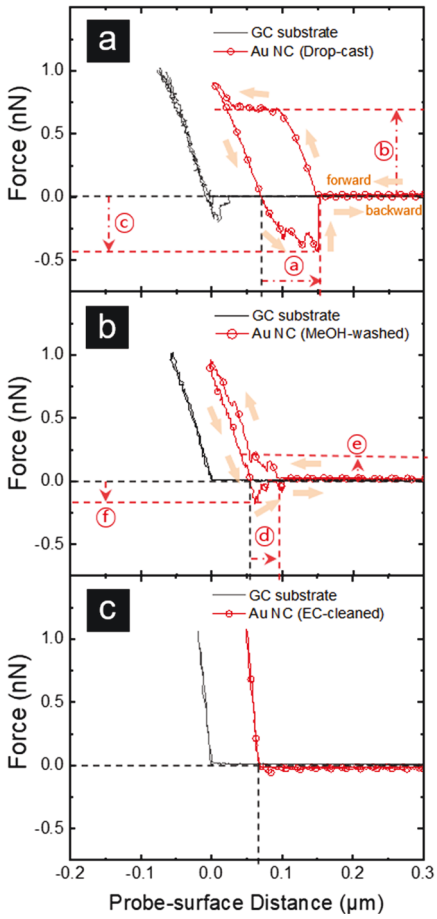

Figure 4. FD curves obtained at a drop-cast (a), MeOH-washed (b), and EC-cleaned (c) Au NC in H_2O. The start of interaction between the tip and interface was determined by measuring the difference between the onset of force at the approaching (forward) and retracting (backward) step of the FD curve in Au NCs (ⓐ and ⓓ). Yield force was measured by the force between the zero-force and plateau region (ⓑ and ⓔ). Maximum adhesion force values were determined by measuring the difference of force between zero-force and the most negative force reached (ⓒ and ⓕ). The approach/retract rate from FD curve acquisition was 1.0 μm/s. Yield and adhesion forces were not detected in EC-cleaned Au NCs (c).

With the measurements described above, information can be extracted regarding the state of adsorbed CTAB for drop-cast, MeOH-washed, and EC-cleaned Au NC samples. Importantly, on the basis of measurements here, we cannot clearly identify monolayer, micelle, bicelle, or extended organized CTAB structures. Considering a bilayer thickness for CTAB of 3.2 nm,[41] the thickness attributed to CTAB at Au NCs in drop-cast sample is in significant excess of what a single bilayer coating would represent, while MeOH-washed and EC-cleaned samples show less than a bilayer. Drop-casting the sample for initial deposition clearly occurs with an excess of CTAB, which then coats the GC substrate and as the solution evaporates, appears to concentrate CTAB in unorganized aggregates at Au NCs.

Ex Situ Measurements of CTAB on Au NCs. Au NCs provide a model system for verifying correlative nanoscale measurements reported here. In particular, the cubic geometry with identical edge lengths along the *x*-, *y*-, and *z*-axes proves beneficial for the correlation of topography from in situ AFM and 2D images from SEM. Au NCs used here had an edge length of 77.5 ± 2.0 nm and an aspect ratio of 1.03, determined by statistical analysis of ca. 100 NCs (Figures S1 and S2).

Here, SEM was utilized as a benchmark EM technique to study adsorbed CTAB on Au NCs in dehydrated conditions. In electron micrographs, the core Au NC and CTAB can be distinguished based on differences in contrast. The adsorbed CTAB thickness decreased over the series of CTAB removal treatments. Compared to untreated drop-cast Au NCs (Figure 2a,d), MeOH-washed Au NCs showed thinner outer layers with rougher morphology and no dark interfacial regions (Figure 2b,e). This contrast was not observed for EC-cleaned Au NCs, suggesting electrochemical cycling was effective at removing a majority of CTAB present (Figure 2c,f). Instead, a thin, rough surface layer attributed to Au/Pd was observed (Figures 2c and S12). The average width of Au NCs after subtracting the Au/Pd layer thickness was calculated as 78.6 and 78.7 nm from the *x*- and *y*-axes, respectively (Table S3), in good agreement with the edge length of Au NCs measured from TEM. Consistency in nanocrystal morphology before and after ligand removal is an important point to confirm. While less aggressive methods, like ligand exchange[42] or chemical washing,[43] are known to preserve nanoparticle structure, more aggressive methods, such as thermal annealing[44,45] or UV-ozone treatment with annealing,[46] can alter nanoparticle morphology. The sequential combination of chemical washing and electrochemical treatment provides a strategy for ligand removal with a minimal obvious change in nanoparticle morphology, with the caveat that, infrequently, some high aspect particle features (corners) were observed to blunt after electrochemical cycling.

To collect electron micrographs with improved contrast between the Au core and CTAB, both in-lens and Everhart–Thornley (ET) detectors were utilized. For drop-cast Au NCs, the contrast difference between the Au NC and CTAB was clearly resolved from both detectors (Figure 2a,d). However, for MeOH-washed samples, adsorbed CTAB was distinguished more easily by the ET detector (Figure 2b,e). Electron micrographs recorded by the in-lens detector are mainly composed of secondary electrons generated from direct excitation by the primary electron beam and originate from small escape depths close to the sample surface. Consequently, images from the in-lens detector have high surface sensitivity and have been used previously to examine surface contamination.[47,48] The ET detector signal originates from secondary electrons generated from interactions of back-scattered electrons with the sample or surrounding materials, generating images from higher kinetic energy electrons with less surface sensitivity.[47] In the measurements here, the contrast between the Au/Pd layer and CTAB in MeOH-washed samples was not clear in the in-lens detector, as opposed to the case of drop-cast Au NC (Figure 2b). Thus, electron micrographs recorded by the ET detector were used for analyzing MeOH-washed samples. CTAB was not obvious in EC-cleaned Au NC images collected with either detector, only a layer typical of the Au/Pd coating. Finally, line profiles from SEM images of three different samples demonstrate that the width of features decreased as sequential surface cleaning steps were conducted, which is attributed to progressive removal of CTAB (Figure 2a′–f′).

In Situ Measurements of CTAB at Au NCs. For applications such as catalysis or biosensing, nanoparticles (NPs) are typically utilized under hydrated conditions. Thus,

https://doi.org/10.1021/acs.langmuir.1c00694
Langmuir 2021, 37, 7701–7711

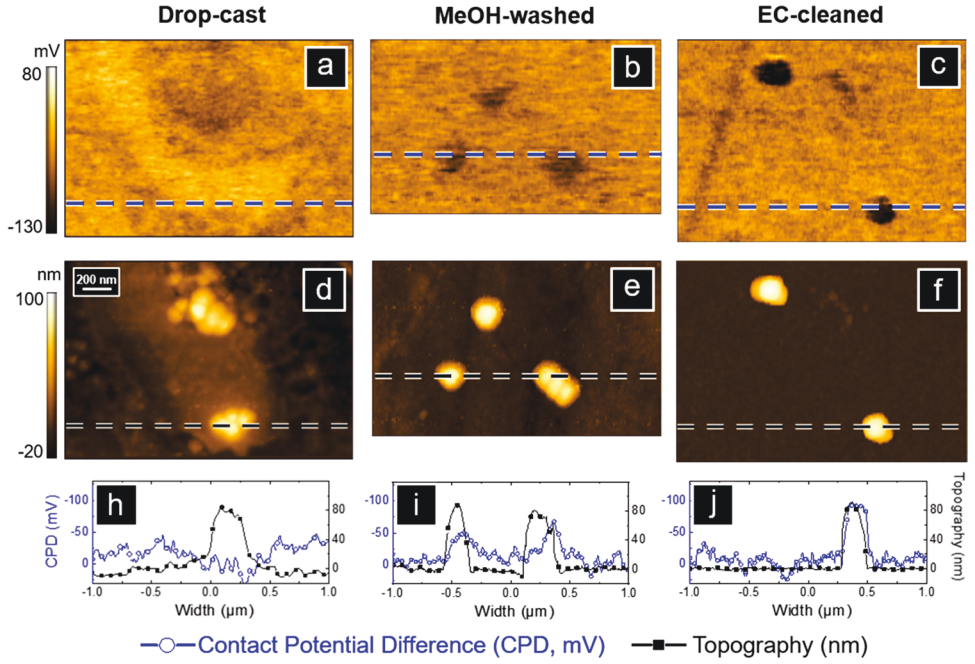

Figure 5. Contact potential difference (CPD) of drop-cast (a), MeOH-washed (b), and EC-cleaned (c) Au NCs, measured by Kelvin probe force microscopy (KPFM), and corresponding topographies (d–f), respectively. The line profile of CPD (blue trace) and topography (black trace) in (h), (i), and (j), respectively, plotted for each sample. The scale bar in (d) is valid for all images.

there are limits to the utility of information extracted from electron microscopy and studying NPs under hydrated conditions is crucial to bridge the gap between the two different environments. Here, in situ AFM was used to characterize adsorbed CTAB thicknesses on Au NCs at the nanometer scale. Information from AFM comes chiefly from three criteria, maximum height, FWHM, and FD spectroscopy. Given an edge length for Au NCs of 77.5 ± 2.0 nm (from TEM), measured height differences for drop-cast, MeOH-washed, and EC-cleaned Au NC samples were ca. 10, 2, and 1 nm of CTAB layer thickness, respectively.

Lateral thicknesses of the CTAB layer were estimated by subtracting the average edge length from the measured width (at FWHM) in AFM measurements and yielded lateral thicknesses of ca. 78, 29, and 13 nm for drop-cast, MeOH-washed, and EC-cleaned samples, respectively. Lateral dimensions of Au NCs measured by AFM in the manner employed here are subject to imaging artifacts, which are important to consider. To rule out convolution of the tip sample, deconvolution under conditions used here was considered. The AFM tip used in this study showed a measured diameter of 8 nm and a tip-surface angle of 10° (Figure S16). When the height of the object is larger than the tip radius, apparent widths are exaggerated due to the interaction of the AFM tip and object, an effect that is exacerbated for objects with sharp features, such as nanocubes imaged here.[49] Since the height of Au NCs is clearly larger (ca. 20 times) than the tip radius, the tip-surface angle is a primary driver of observed artifacts. The sidewall angle in the topographies of drop-cast, MeOH-washed, and EC-cleaned Au NCs was 30, 24, and 20°, respectively, which are greater than the tip-surface angle (Figure S17), suggesting that the topographies in all three conditions were not affected by tip artifacts during imaging. To verify further, tip-deconvolution analysis was carried out with an 8 nm tip diameter and varied tip sidewall angles in the range from 5 to 40° for both topographies of drop-cast and EC-cleaned Au NCs (Figure S18). The line profile change was negligible in drop-cast Au NCs (Figure S18a) after tip-deconvolution at angles as high as 40°. In EC-cleaned Au NCs (Figure S18b), attempts to further deconvolute images by increasing the sidewall angle decreased the width at the top surface of Au NCs to values below ca. 77.5 nm (from TEM), which is physically unrealistic based on EM characterization. We should note that we cannot exclusively rule out adsorption of CTAB to the tip of the AFM cantilever, which could lead to lateral broadening. Results from FD spectroscopy, in particular, show interaction of a hard tip with a hard surface, which suggests that there is little or no CTAB at the cantilever tip.

AFM imaging in liquid is known to decrease resolution, a consequence of both a lower *Q*-factor and a less well-defined resonance frequency. In air, where *Q*-factors can be more readily characterized, tapping mode AFM shows high sensitivity to equilibrium perturbations when the tip reaches a sharp vertical edge,[50] the same as what would be expected for a perfectly clean Au NC, which likely limits lateral resolution for these samples. Additionally, in an effort to minimize interference from residual salts in subsequent EM imaging, an electrolyte was not added to solutions used here. The lack of an electrolyte means electrostatic forces between the tip and sample may not be effectively screened. The opportunity for additional chemical interactions between the tip and sample also exists, especially for the case of drop-cast and MeOH-washed samples, where CTAB molecules initially adsorbed on the surface can equilibrate with bulk solution and then may adsorb to the AFM probe. With these caveats in mind, and comparative data from SEM, high confidence exists that excess CTAB is present in the case of both drop-cast and MeOH-washed samples. For the EC-cleaned sample, the presence of CTAB at Au NC sidewalls is unclear.

Measurements from FD spectroscopy provide additional information related to the nature of CTAB present. Previous

https://doi.org/10.1021/acs.langmuir.1c00694
Langmuir 2021, 37, 7701−7711

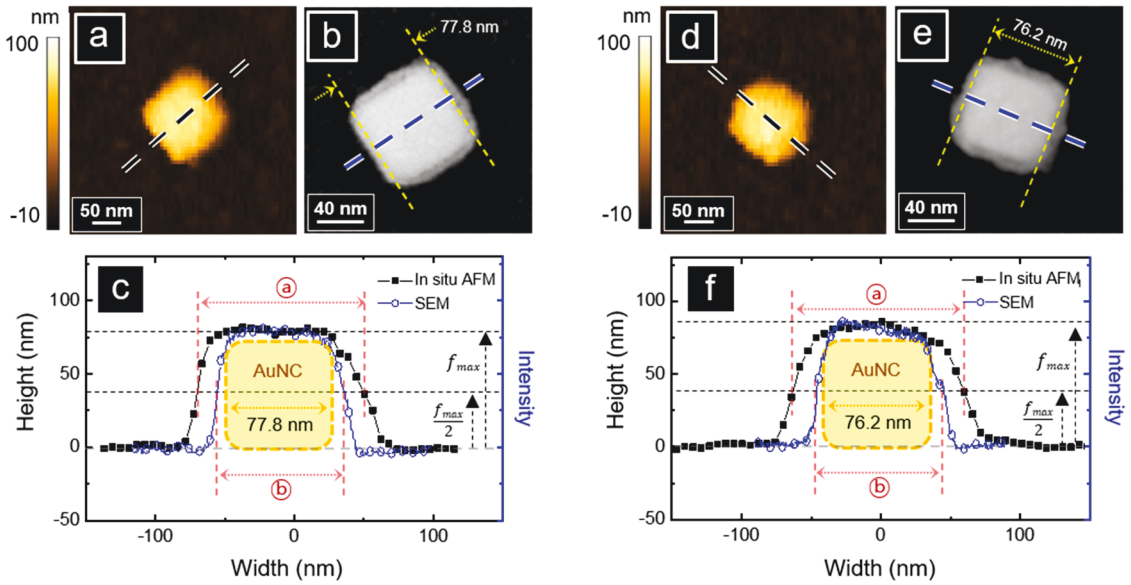

Figure 6. Representative examples of correlative in situ AFM and SEM characterization of MeOH-washed Au NCs. AFM topography (a) (scan size: 380 nm × 380 nm) and corresponding electron micrograph (b) of the Au NC. The edge length of the Au NC was measured between yellow-dashed lines illustrated in (b). Cross-sectional view (c) of Au NC measured by in situ AFM (black trace) and SEM (blue trace). The in situ AFM line profile was collected along the black dashed line in (a), and the SEM line profile was collected along the blue dashed line in (b). Width measured for both in situ AFM and SEM were defined by FWHM (ⓐ and ⓑ). Additional samples described were characterized in a similar fashion (d–f).

FD measurements at mica surfaces have reported the start of measurable interactions at distances of <10 nm for CTAB and CTAC on hydrophilic mica surfaces.[14,15] For Au NCs measured here, interaction start distances of ca. 80 and 40 nm were measured for drop-cast and MeOH-washed Au NCs, respectively, which are both significantly longer than that measured previously (Figure 4), likely due to the fact that in previous studies, ordered layers were investigated and the electrolyte added to the solution screened electrostatic forces present. In sum, interaction start distance, yield force, and adhesion force from the interaction of AFM tip with adsorbed CTAB were all reduced after methanol treatment and disappeared with electrochemical cleaning.

KPFM Measurements. Observations here of different CTAB thicknesses at Au NCs underscore the importance of considering sample quality in the evaluation of solution-processed nanomaterials used in catalysis, both in terms of the electrochemical surface area and of the contact between the nanoparticle and underlying substrate. Such effects have been discussed previously in studies, for instance by Wang and co-workers, which showed a poor electrical contact between NP catalysts and the electrode surface could result in significant differences in electrochemical activity.[51] Moreover, residual CTAB could possibly influence selectivity in catalytic reactions under some circumstances.[7] KPFM provides a route to probe the electrical properties of drop-cast, MeOH-washed, and EC-cleaned samples (Figure 5).

Previous studies have taken advantage of KPFM to evaluate the influence of surface adsorbates at the submicron scale. For instance, Abdellatif et al.[52] demonstrated that a capping agent, oleylamine, significantly affected surface-potential measurements of Au nanoparticles. Thermal annealing was used to remove oleylamine, which resulted in significant particle aggregation. In results here, KPFM measurements compared to topographic measurements are informative of the electrical properties of Au NCs before and after cleaning steps. In the drop-cast sample, CPD values were nonexistent, or possibly even depressed over areas that are assumed to be Au NCs. For MeOH-washed samples, maximal CPD values were depressed (ca. −50 mV) and showed correlation with Au NCs in topography, but the response was broader than the actual Au NC width. For EC-cleaned samples, a more significant CPD response was measured (ca. −90 mV) and CPD response tracked well with the lateral dimensions of Au NCs. These results indicate that removal of insulating CTAB layers through the cleaning methods here improves nanoscale electrical contact with the sample.

Correlative AFM and SEM. Correlative measurements of in situ AFM and in vacuo SEM provide a deeper understanding of adsorbed CTAB on Au NCs by investigating the same Au NC under two different environments, dehydrated and hydrated conditions. The correlative analysis also provides more reliable measurements by minimizing potential errors from subtle size variation of synthesized Au NCs. For instance, from the AFM measurements of maximum height (Table 2), CTAB thickness was determined to be 2.1 and 1.3 nm for MeOH-washed and EC-cleaned Au NCs, respectively. However, the measured thickness is within a standard deviation of the edge length of Au NC itself, which is ca. 2.0 nm determined from analyzing TEM images (Figure S1). Here in correlative studies, the edge length of the same Au NC can be determined from SEM, minimizing error, and allowing heterogeneity of CTAB adsorption on Au NCs to be studied more reliably.

Heterogeneity in the presence of CTAB was measured by comparison of individual MeOH-washed Au NCs with correlative SEM and AFM measurements. Typically, a 10 μm × 10 μm scan was recorded by in situ AFM, followed by SEM of the same area (Figure S19). Figure 6 presents two representative sets of data analyzed via correlative measurement techniques (additional data included in Figure S20 and Table S7). To compare CTAB thickness under the two

https://doi.org/10.1021/acs.langmuir.1c00694
Langmuir 2021, 37, 7701−7711

conditions, line profiles from AFM (black trace) and SEM (blue trace) were extracted from the corresponding images of Figure 6a,b, respectively, then plotted together in Figure 6c. The core diameter of the Au NC (edge length) was measured from SEM images as shown with the yellow-dashed line in Figure 6b, where the edge length and height are taken as 77.8 nm. The intensity value from the SEM image was adjusted to match the maximum height of the in situ AFM line profile for proper comparison of the width of adsorbed CTAB. AFM showed 79.9 nm height which is 2.1 nm greater than the edge length of Au NC determined by SEM. Accordingly, six additional Au NCs from the same scan area showed CTAB thickness in hydrated conditions that varied from 1.8 to 6.8 nm, except for one Au NC (#1, Table S7), which is possibly a result of a misshaped particle. Meanwhile, variation in the lateral CTAB thickness measured from FWHM of Au NCs was greater than in height measurements. CTAB thickness under hydrated conditions was calculated by subtracting the edge length (from SEM) of the Au NC from the measured FWHM, while that under dehydrated conditions was determined by subtracting the edge length of Au NC and the Au/Pd coating thickness from the measured width. Consequently, under hydrated conditions, a CTAB thickness of 21.1 nm (FWHM) was measured by in situ AFM (ⓐ in Figure 6c), while that under dehydrated conditions was 2.6 nm on the line profile measured by SEM (ⓑ in Figure 6c). As an example, a second Au NC (Figure 6d–f) showed the same trend as observed in Figure 6a–c, with six other individual single Au NCs showing CTAB thicknesses that vary from 13.4 to 22.3 nm from AFM and from 0.1 to 3.9 nm from SEM (Table S8), which further underscores heterogeneity in terms of the amount of CTAB present on different particles. Correlative results shown in Figure 6 also clearly demonstrate that for the same Au NC, adsorbed CTAB appears thicker under hydrated conditions than dehydrated conditions.

CONCLUSIONS

We have characterized the stepwise ligand removal of CTAB at individual Au NCs using a battery of AFM and SEM techniques, including correlative in situ AFM and SEM measurements. Significant amounts of CTAB were detected by AFM and EM after methanol washing alone. Electrochemical cycling was demonstrated as a possible method to remove CTAB ligands from Au NCs.

The presence of CTAB after all cleaning steps is the most important point to consider. For EC-cleaned Au NCs, results here suggest the following. First, the presence of CTAB on the sidewalls of Au NCs remains a possibility but is inconclusive. Second, the maximum height of EC-cleaned Au NCs (Table 2, ca. 78.8 nm) is nearly identical to the average edge length of pristine Au NCs (Figure S1, ca. 77.5 nm) and well within the standard deviation (±2.0 nm) of the average. Third, FD results also do not reveal the presence of a significant layer at the top of the Au NC. Height measurements give values that are well within the inherent statistical deviations of particle dimensions and asymmetry from TEM, which combined with FD measurements suggests the possibility of complete removal of CTAB. However, we cannot exclusively rule out the presence of residual CTAB, which could reside at the interface between the GC surface and the Au NC. The supposition that residual CTAB might reside at the interface between Au NCs and surfaces seems a possibility given the methods used here to remove CTAB likely may not completely access the hindered physical space underneath Au NCs. Fourth, and to the issue of the impact of the presence of CTAB at the Au NC–GC interface, KPFM data showed markedly improved correlation between topographic response and CPD measurements after EC-cleaning.

These results suggest that complete removal of CTAB on Au NCs is not always trivial, and we expect that this is a generalizable conclusion that should be considered when working with nanomaterials and surfactants. Clearly, the presence of residual ligands should be considered even if no signal is observed from common EM or FT-IR spectroscopy. Collectively, the single-particle analysis framework described here paves the way to assessing the efficacy of ligand removal on individual nanoscale catalysts and underscores the importance of considering the surface chemistry in applications of solution synthesized nanomaterials.

ASSOCIATED CONTENT

Supporting Information

The Supporting Information is available free of charge at https://pubs.acs.org/doi/10.1021/acs.langmuir.1c00694.

Synthesis and experimental details, description of in situ AFM, in situ FD spectroscopy, and electron micrographs (PDF)

AUTHOR INFORMATION

Corresponding Authors

Xingchen Ye – *Department of Chemistry, Indiana University, Bloomington, Indiana 47405, United States;* orcid.org/0000-0001-6851-2721; Phone: +1-812-855-6011; Email: xingye@indiana.edu

Lane A. Baker – *Department of Chemistry, Indiana University, Bloomington, Indiana 47405, United States;* orcid.org/0000-0001-5127-507X; Phone: +1-812-856-1873; Email: lanbaker@indiana.edu

Authors

Myung-Hoon Choi – *Department of Chemistry, Indiana University, Bloomington, Indiana 47405, United States*

Soojin Jeong – *Department of Chemistry, Indiana University, Bloomington, Indiana 47405, United States*

Yi Wang – *Department of Chemistry, Indiana University, Bloomington, Indiana 47405, United States*

Sang-Joon Cho – *Park Systems Corporation, Suwon 16229, Korea*

Sang-Il Park – *Park Systems Corporation, Suwon 16229, Korea*

Complete contact information is available at: https://pubs.acs.org/10.1021/acs.langmuir.1c00694

Author Contributions

M.-H.C., S.J., and Y.W. performed experiments. M.-H.C., S.-J.C., S.-I.P., X.Y., and L.A.B. wrote the manuscript.

Funding

M.-H.C. and L.A.B. acknowledge support from the National Science Foundation (CHE-1808133). S.J., Y.W., and X.Y. acknowledge support from the U.S. National Science Foundation (NSF DMR-2102526).

Notes

The authors declare no competing financial interest.

■ ACKNOWLEDGMENTS

The IU Nanoscale Characterization Facility is acknowledged for access to and use of the scanning electron microscope (obtained through the National Science Foundation MRI program (CHE-0923064)). Park Systems is gratefully acknowledged for access to instrumentation used to obtain AFM data.

■ ABBREVIATIONS

Au NCs, gold nanocubes; CTAB, cetyltrimethylammonium bromide; in situ AFM, in situ atomic force microscopy; SEM, scanning electron microscopy; FD, force−distance spectroscopy; GC, glassy carbon; KPFM, Kelvin probe force microscopy

■ REFERENCES

(1) Xia, Y.; Xiong, Y.; Lim, B.; Skrabalak, S. E. Shape-controlled Synthesis of Metal Nanocrystals: Simple Chemistry Meets Complex Physics? *Angew. Chem., Int. Ed.* **2009**, *48*, 60−103.
(2) Nikoobakht, B.; El-Sayed, M. A. Evidence for Bilayer Assembly of Cationic Surfactants on the Surface of Gold Nanorods. *Langmuir* **2001**, *17*, 6368−6374.
(3) Nikoobakht, B.; El-Sayed, M. A. Preparation and Growth Mechanism of Gold Nanorods (NRs) Using Seed-Mediated Growth Method. *Chem. Mater.* **2003**, *15*, 1957−1962.
(4) Sau, T. K.; Murphy, C. J. Self-Assembly Patterns Formed upon Solvent Evaporation of Aqueous Cetyltrimethylammonium Bromide-Coated Gold Nanoparticles of Various Shapes. *Langmuir* **2005**, *21*, 2923−2929.
(5) Garabagiu, S.; Bratu, I. Thiol Containing Carboxylic Acids Remove the CTAB Surfactant Onto the Surface of Gold Nanorods: An FTIR Spectroscopic Study. *Appl. Surf. Sci.* **2013**, *284*, 780−783.
(6) Yang, T. H.; Shi, Y.; Janssen, A.; Xia, Y. Surface Capping Agents and Their Roles in Shape-Controlled Synthesis of Colloidal Metal Nanocrystals. *Angew. Chem., Int. Ed.* **2020**, *59*, 15378−15401.
(7) Zhang, Z. Q.; Banerjee, S.; Thoi, V. S.; Hall, A. S. Reorganization of Interfacial Water by an Amphiphilic Cationic Surfactant Promotes CO_2 Reduction. *J. Phys. Chem. Lett.* **2020**, *11*, 5457−5463.
(8) Banerjee, S.; Han, X.; Thoi, V. S. Modulating the Electrode−Electrolyte Interface with Cationic Surfactants in Carbon Dioxide Reduction. *ACS Catal.* **2019**, *9*, 5631−5637.
(9) Lu, L.; Zou, S.; Zhou, Y.; Liu, J.; Li, R.; Xu, Z.; Xiao, L.; Fan, J. Ligand-regulated ORR Activity of Au Nanoparticles in Alkaline Medium: the Importance of Surface Coverage of Ligands. *Catal. Sci. Technol.* **2018**, *8*, 746−754.
(10) Kim, D.; Yu, S.; Zheng, F.; Roh, I.; Li, Y.; Louisia, S.; Qi, Z.; Somorjai, G. A.; Frei, H.; Wang, L.-W.; Yang, P. Selective CO_2 Electrocatalysis at the Pseudocapacitive Nanoparticle/Ordered-ligand Interlayer. *Nat. Energy* **2020**, *5*, 1032−1042.
(11) Choi, M.-H.; Siepser, N. P.; Jeong, S.; Wang, Y.; Jagdale, G.; Ye, X.; Baker, L. A. Probing Single-Particle Electrocatalytic Activity at Facet-Controlled Gold Nanocrystals. *Nano Lett.* **2020**, *20*, 1233−1239.
(12) Baker, L. A. Perspective and Prospectus on Single-Entity Electrochemistry. *J. Am. Chem. Soc.* **2018**, *140*, 15549−15559.
(13) Manne, S.; Gaub, H. E. Molecular Organization of Surfactants at Solid-Liquid Interfaces. *Science* **1995**, *270*, 1480−1482.
(14) Lamont, R. E.; Ducker, W. A. Surface-Induced Transformations for Surfactant Aggregates. *J. Am. Chem. Soc.* **1998**, *120*, 7602−7607.
(15) Rabinovich, Y. I.; Vakarelski, I. U.; Brown, S. C.; Singh, P. K.; Moudgil, B. M. Mechanical and Thermodynamic Properties of Surfactant Aggregates at the Solid−Liquid Interface. *J. Colloid Interface Sci.* **2004**, *270*, 29−36.
(16) Janicek, B. E.; Hinman, J. G.; Hinman, J. J.; Bae, S.; Wu, M.; Turner, J.; Chang, H.-H.; Park, E.; Lawless, R.; Suslick, K. S.; Murphy, C. J.; Huang, P. Y. Quantitative Imaging of Organic Ligand Density on Anisotropic Inorganic Nanocrystals. *Nano Lett.* **2019**, *19*, 6308−6314.
(17) Kim, J.-Y.; Han, M.-G.; Lien, M.-B.; Magonov, S.; Zhu, Y.; George, H.; Norris, T. B.; Kotov, N. A. Dipole-like Electrostatic Asymmetry of Gold Nanorods. *Sci. Adv.* **2018**, *4*, No. e1700682.
(18) Ge, Y.; Liu, J.; Liu, X.; Hu, J.; Duan, X.; Duan, X. Rapid Electrochemical Cleaning Silver Nanowire Thin Films for High-Performance Transparent Conductors. *J. Am. Chem. Soc.* **2019**, *141*, 12251−12257.
(19) Bong, S.; Jang, B.; Han, D.; Piao, Y. Effective Electrochemical Activation of Oleate-Residue-Fouled Pt Nanoparticle Catalysts for Methanol and Formic Acid Oxidation. *ACS Omega* **2019**, *4*, 20330−20334.
(20) Lu, L.; Lou, B.; Zou, S.; Kobayashi, H.; Liu, J.; Xiao, L.; Fan, J. Robust Removal of Ligands from Noble Metal Nanoparticles by Electrochemical Strategies. *ACS Catal.* **2018**, *8*, 8484−8492.
(21) Martín-Yerga, D.; Costa-Garcia, A.; Unwin, P. R. Correlative Voltammetric Microscopy: Structure-Activity Relationships in the Microscopic Electrochemical Behavior of Screen Printed Carbon Electrodes. *ACS Sens.* **2019**, *4*, 2173−2180.
(22) Ornelas, I. M.; Unwin, P. R.; Bentley, C. L. High-Throughput Correlative Electrochemistry-Microscopy at a Transmission Electron Microscopy Grid Electrode. *Anal. Chem.* **2019**, *91*, 14854−14859.
(23) Nakajima, M.; Mizutani, Y.; Iwata, F.; Ushiki, T. Scanning Ion Conductance Microscopy for Visualizing the Three-dimensional Surface Topography of Cells and Tissues. *Semin. Cell Dev. Biol.* **2018**, *73*, 125−131.
(24) Ushiki, T.; Nakajima, M.; Choi, M.-H.; Cho, S.-J.; Iwata, F. Scanning Ion Conductance Microscopy for Imaging Biological Samples in Liquid: A Comparative Study with Atomic Force Microscopy and Scanning Electron Microscopy. *Micron* **2012**, *43*, 1390−1398.
(25) Caplan, J.; Niethammer, M.; Taylor, R. M.; Czymmek, K. J. The Power of Correlative Microscopy: Multi-modal, Multi-scale, Multi-dimensional. *Curr. Opin. Struct. Biol.* **2011**, *21*, 686−693.
(26) Rangelow, I. W.; Kaestner, M.; Ivanov, T.; Ahmad, A.; Lenk, S.; Lenk, C.; Guliyev, E.; Reum, A.; Hofmann, M.; Reuter, C.; Holz, M. Atomic Force Microscope Integrated with A Scanning Electron Microscope for Correlative Nanofabrication and Microscopy. *J. Vac. Sci. Technol. B* **2018**, *36*, No. 06J102.
(27) Sarvghad-Moghaddam, M.; Parvizi, R.; Davoodi, A.; Haddad-Sabzevar, M.; Imani, A. Establishing a Correlation Between Interfacial Microstructures and Corrosion Initiation Sites in Al/Cu Joints by SEM−EDS and AFM−SKPFM. *Corros. Sci.* **2014**, *79*, 148−158.
(28) Niu, W.; Zheng, S.; Wang, D.; Liu, X.; Li, H.; Han, S.; Chen, J.; Tang, Z.; Xu, G. Selective Synthesis of Single-crystalline Rhombic Dodecahedral, Octahedral, and Cubic Gold Nanocrystals. *J. Am. Chem. Soc.* **2009**, *131*, 697−703.
(29) O'Brien, M. N.; Jones, M. R.; Brown, K. A.; Mirkin, C. A. Universal Noble Metal Nanoparticle Seeds Realized Through Iterative Reductive Growth and Oxidative Dissolution Reactions. *J. Am. Chem. Soc.* **2014**, *136*, 7603−7606.
(30) Shikata, T.; Hirata, H.; Kotaka, T. Micelle Formation of Detergent Molecules in Aqueous Media: Viscoelastic Properties of Aqueous Cetyltrimethylamonium Bromide Solution. *Langmuir* **1987**, *3*, 1081−1086.
(31) Bielawska, M.; Chodzińska, A.; Jańczuk, B.; Zdziennicka, A. Determination of CTAB CMC in Mixed Water+Short-chain Alcohol Solvent by Surface Tension, Conductivity, Density and Viscosity Measurements. *Colloids Surf., A* **2013**, *424*, 81−88.
(32) González-Rivera, J.; Tovar-Rodríguez, J.; Bramanti, E.; Duce, C.; Longo, I.; Fratini, E.; Galindo-Esquivel, I. R.; Ferrari, C. Surfactant Recovery from Mesoporous Metal-modified Materials (Sn-, Y-, Ce-, Si-MCM-41), by Ultrasound Assisted Ion-exchange Extraction and Its Re-use for a Microwave In Situ Cheap and Eco-friendly MCM-41 Synthesis. *J. Mater. Chem. A* **2014**, *2*, 7020−7033.
(33) Schneider, C. A.; Rasband, W. S.; Eliceiri, K. W. NIH Image to ImageJ: 25 Years of Image Analysis. *Nat. Methods* **2012**, *9*, 671−675.
(34) Kim, J.; Choi, M.-H.; Jung, G.-E.; Ferhan, A. R.; Cho, N.-J.; Cho, S.-J. Dimensional Comparison Between Amplitude-modulation

https://doi.org/10.1021/acs.langmuir.1c00694
Langmuir 2021, 37, 7701−7711

Atomic Force Microscopy and Scanning Ion Conductance Microscopy of Biological Samples. *Jpn. J. Appl. Phys.* **2016**, *55*, No. 08NB18.
(35) Choi, M.-H.; Baker, L. A. Biphasic-Scanning Ion Conductance Microscopy. *Anal. Chem.* **2018**, *90*, 11797−11801.
(36) Usukura, J.; Yoshimura, A.; Minakata, S.; Youn, D.; Ahn, J.; Cho, S.-J. Use of the Unroofing Technique for Atomic Force Microscopic Imaging of the Intra-cellular Cytoskeleton under Aqueous Conditions. *J. Electron Microsc.* **2012**, *61*, 321−326.
(37) Roh, H. S.; Lee, C. M.; Hwang, Y. H.; Kook, M. S.; Yang, S. W.; Lee, D.; Kim, B. H. Addition of MgO Nanoparticles and Plasma Surface Treatment of Three-dimensional Printed Polycaprolactone/Hydroxyapatite Scaffolds for Improving Bone Regeneration. *Mater. Sci. Eng. C* **2017**, *74*, 525−535.
(38) Purcar, V.; Rădiţoiu, V.; Dumitru, A.; Nicolae, C.-A.; Frone, A. N.; Anastasescu, M.; Rădiţoiu, A.; Raduly, M. F.; Gabor, R. A.; Căprărescu, S. Antireflective Coating Based on TiO_2 Nanoparticles Modified with Coupling Agents via Acid-Catalyzed Sol-Gel Method. *Appl. Surf. Sci.* **2019**, *487*, 819−824.
(39) Nečas, D.; Klapetek, P. Gwyddion: an Open-source Software for SPM Data Analysis. *Cent. Eur. J. Phys.* **2012**, *10*, 181−188.
(40) Zhand, S.; Razmjou, A.; Azadi, S.; Bazaz, S. R.; Shrestha, J.; Jahromi, M. A. F.; Warkiani, M. E. Metal−Organic Framework-Enhanced ELISA Platform for Ultrasensitive Detection of PD-L1. *ACS Appl. Bio Mater.* **2020**, *3*, 4148−4158.
(41) Gómez-Graña, S.; Hubert, F.; Testard, F.; Guerrero-Martinez, A.; Grillo, I.; Liz-Marzan, L. M.; Spalla, O. Surfactant (Bi)Layers on Gold Nanorods. *Langmuir* **2012**, *28*, 1453−1459.
(42) Zhou, C.; Bai, Y.; Yang, F.; Sun, T.; Zhang, L.; Cai, Y.; Gu, T.; Liu, Y.; Gong, M.; Zhang, D.; Yin, Y. Ligand Exchange on Noble Metal Nanocrystals Assisted by Coating and Etching of Cuprous Oxide. *Mater. Chem. Front.* **2020**, *4*, 1614−1622.
(43) Wang, C.; Daimon, H.; Onodera, T.; Koda, T.; Sun, S. A General Approach to the Size- and Shape-controlled Synthesis of Platinum Nanoparticles and Their Catalytic Reduction of Oxygen. *Angew. Chem., Int. Ed.* **2008**, *47*, 3588−3591.
(44) Brimaud, S.; Coutanceau, C.; Garnier, E.; Léger, J. M.; Gérard, F.; Pronier, S.; Leoni, M. Influence of Surfactant Removal by Chemical or Thermal Methods on Structure and Electroactivity of Pt/C Catalysts Prepared by Water-in-oil Microemulsion. *J. Electroanal. Chem.* **2007**, *602*, 226−236.
(45) Yu, R.; Song, H.; Zhang, X.-F.; Yang, P. Thermal Wetting of Platinum Nanocrystals on Silica Surface. *J. Phys. Chem. B* **2005**, *109*, 6940−6943.
(46) Niu, Z.; Li, Y. Removal and Utilization of Capping Agents in Nanocatalysis. *Chem. Mater.* **2014**, *26*, 72−83.
(47) Zhang, X.; Cen, X.; Ravichandran, R.; Hughes, L. A.; van Benthem, K. Simultaneous Scanning Electron Microscope Imaging of Topographical and Chemical Contrast Using In-Lens, In-Column, and Everhart−Thornley Detector Systems. *Microsc. Microanal.* **2016**, *22*, 565−575.
(48) Griffin, B. J. A Comparison of Conventional Everhart-Thornley Style and In-lens Secondary Electron Detectors: a Further Variable in Scanning Electron Microscopy. *Scanning* **2011**, *33*, 162−173.
(49) Canet-Ferrer, J.; Coronado, E.; Forment-Aliaga, A.; Pinilla-Cienfuegos, E. Correction of the Tip Convolution Effects in the Imaging of Nanostructures Studied through Scanning Force Microscopy. *Nanotechnology* **2014**, *25*, No. 395703.
(50) Eves, B. J.; Green, R. G. Limitations on Accurate Shape Determination using Amplitude Modulation Atomic Force Microscopy. *Ultramicroscopy* **2012**, *115*, 14−20.
(51) Wei, W.; Yuan, T.; Jiang, W.; Gao, J.; Chen, H.-Y.; Wang, W. Accessing the Electrochemical Activity of Single Nanoparticles by Eliminating the Heterogeneous Electrical Contacts. *J. Am. Chem. Soc.* **2020**, *142*, 14307−14313.
(52) Abdellatif, M. H.; Ghosh, S.; Liakos, I.; Scarpellini, A.; Marras, S.; Diaspro, A.; Salerno, M. Effect of Nanoscale Size and Medium on Metal Work Function in Oleylamine-capped Gold Nanocrystals. *J. Phys. Chem. Solids* **2016**, *89*, 7−14.

https://doi.org/10.1021/acs.langmuir.1c00694
Langmuir 2021, 37, 7701−7711